Low Temperature, Vacuum-Processed Bismuth Triiodide Solar Cells with Organic Small-Molecule Hole Transport Bilayer

Paz Sebastia-Luna, Michele Sessolo, Francisco Palazon,* and Henk J. Bolink

Herein, the preparation of fully vacuum-processed bismuth triiodide solar cells with low annealing temperature is reported. Planar n-i-p devices are prepared using a thin compact SnO_2 layer as the electron extraction layer and an electron blocking/hole extraction bilayer consisting of an intrinsic and doped organic hole-transport molecule. Using this configuration, herein, higher fill-factors and overall power conversion efficiencies than with conventional solution-processed hole transport materials are achieved.

1. Introduction

Bismuth triiodide has recently been proposed as a promising absorber material for photovoltaic (PV) applications because of its semiconducting nature, high dielectric constant (low exciton binding energy), high defect tolerance, low toxicity and suitable bandgap, which is of interest for the development of front-cell absorbers in tandem configurations.[1,2] This combination of properties makes bismuth triiodide (BiI_3) a potential candidate for next-generation PVs. Nevertheless, despite several reports of solar cells employing BiI_3 as absorber material, their efficiency remains limited due to several factors, among which the inhomogeneous morphology of BiI_3 thin films, a problem already known for other bismuth halides, such as $CsBi_3I_{10}$.[3–5] Traditionally, these films are deposited using solution processing involving organic solvents, such as dimethylformamide (DMF) or dimethyl sulfoxide, and require a high-temperature annealing step (above 120 °C) to reduce the roughness and the presence of pinholes in the layers.[6–9] In fact, the inhomogeneous morphology of the BiI_3 layer has led some authors to investigate a quasi-bulk heterojunction architecture with the infiltration of [6,6]-phenyl-C61-

butyric acid methyl ester inside the porous BiI_3 film.[10] Thermal vacuum deposition of BiI_3 has also been demonstrated, albeit still requiring post-deposition annealing at high temperature.[11–13] Furthermore, another factor that strongly affects the performance of BiI_3-based solar cells is its deep valence band maximum around −5.8 eV, which makes the choice of a proper hole transport layer (HTL) difficult.[14] A wide range of HTLs have been tested so far, such as V_2O_5,[15] $NbSe_x$,[16] PTB7-Th,[8] F8[17] or spiro-MeOTAD,[18] with the last two leading to the highest power conversion efficiency (PCE) reported for a planar heterojunction (1.21% PCE).

Herein, we report the first fabrication of fully vacuum processed BiI_3 solar cells, where only a low-temperature annealing step is required. In short, SnO_2 electron transport layers are grown by atomic-layer deposition (ALD) on patterned indium tin oxide (ITO) on glass substrates. The BiI_3 thin films are deposited by thermal vacuum deposition and annealed at 50 or 100 °C for 10 min. As HTL, we employed a vacuum-deposited bilayer of intrinsic and doped organic small-molecule semiconductor. Specifically, 20 nm of the arylamine derivative N4,N4,N4″,N4″-tetra([1,1′-biphenyl]-4-yl)-[1,1′:4′,1″-terphenyl]-4,4″-diamine (TaTm) is evaporated on BiI_3, followed by 40 nm of the same molecule doped with 2,2′-(Perfluoronaphthalene-2,6-diylidene) dimalononitrile (F_6-TCNNQ). The stack is finished with a gold electrode. The champion device exhibits a PCE of 0.72% (and a fill factor of 51.2%), close to record values for BiI_3 single junction solar cells. Moreover, this outperforms the results obtained with spiro-OMeTAD HTL that we also evaluated for comparison and with which a PCE of 0.54% was achieved.

P. Sebastia-Luna, M. Sessolo, F. Palazon, H. J. Bolink
Instituto de Ciencia Molecular
ICMol
Universidad de Valencia
C/ Catedrático J. Beltrán 2, 46980 Paterna, Spain
E-mail: francisco.palazon@uv.es

The ORCID identification number(s) for the author(s) of this article can be found under https://doi.org/10.1002/ente.202100661.
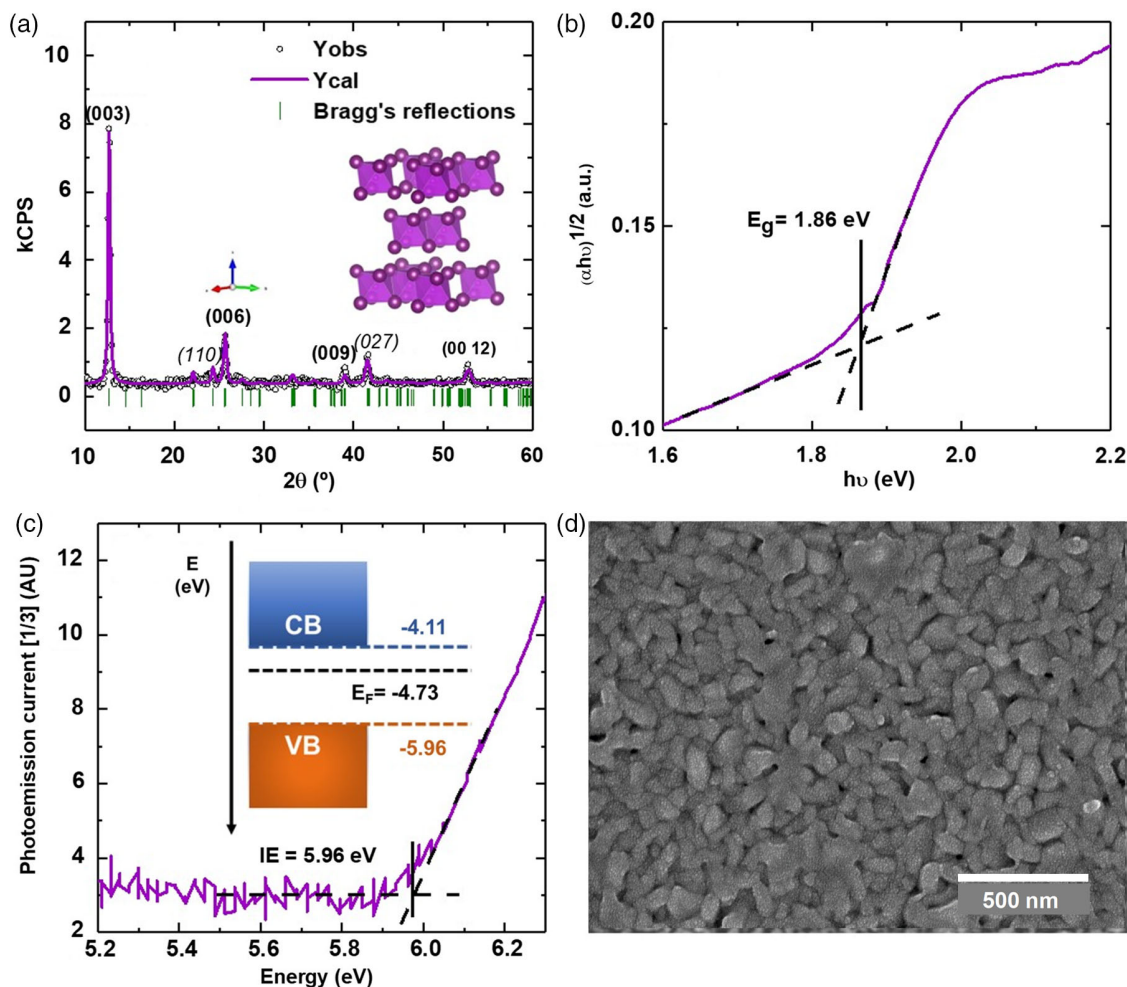
2. Results and Discussion

BiI_3 was deposited by thermal evaporation under high-vacuum conditions (see ESI for further details on the experimental procedure). The X-ray diffractogram of a 100 nm thin film on glass and corresponding whole-pattern Le Bail fit are presented in **Figure 1**a. Experimental data matches well with the expected phase for BiI_3 (R-3 space group)[19] showing no sign of degradation upon evaporation. Furthermore, the film shows a preferential crystalline orientation along the c-axis as noted by the intense (00l) peaks. This corresponds to a preferential growth on the substrate with the layers of edge-sharing $[BiI_6]^{3-}$ octahedra

**ADVANCED
SCIENCE NEWS**

www.advancedsciencenews.com

Energy Technology
Generation, Conversion, Storage, Distribution

www.entechnol.de
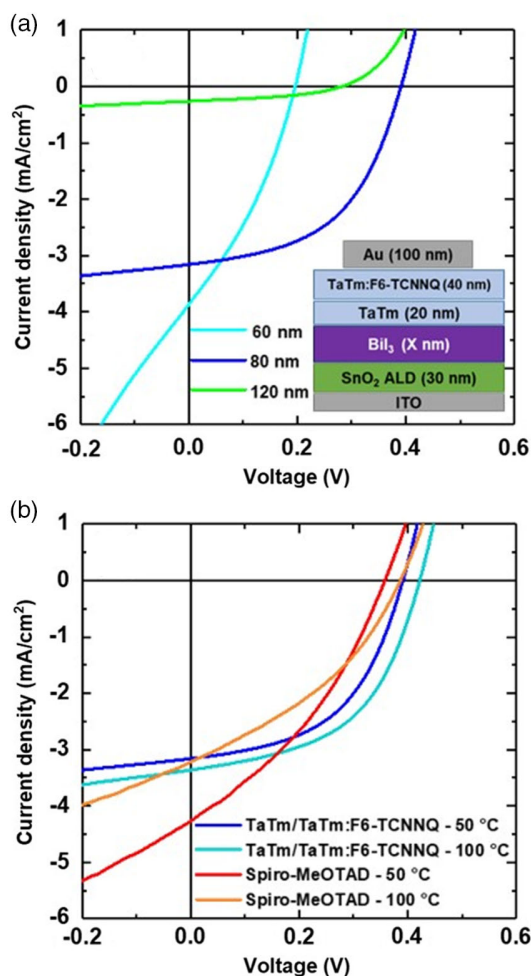
Figure 1. a) XRD diffractogram of BiI$_3$ thin film showing planes with preferential orientation (bold) and secondary orientations (normal). An inset representing the 3D crystalline structure is given. b) Tauc's plot showing the bandgap transition at 1.86 eV. c) Ionization Energy calculated from APS measurement. Band diagram of BiI$_3$ is presented at the inset. d) SEM image of thin film with a scale bar of 500 nm.

perpendicular to the growth direction, as schematically represented in the inset of Figure 1a. UV-Vis absorption spectrum shows a broad absorption band with the characteristic excitonic peak around 2.0 eV, as noted by Kang et al. and Turjanica et al. (Figure S1, Supporting Information).[10,14] From the corresponding Tauc plot it is possible to derive a bandgap energy (E_g) of 1.86 eV (Figure 1b), in agreement with previously reported values.[1,13,14,16] It has also been shown that this value is linked to so-called edge effects present in bulk polycrystalline samples and that single- or multilayer flat BiI$_3$ presents a wider intrinsic bandgap around 2.5 eV.[20] Air photoemission spectroscopy (APS) was performed to gain more insights into the electronic energy level of the films. The ionization potential (corresponding to the valence band maximum; VBM) was found to be −5.96 eV, in close agreement with previous reports (−5.8 eV) where it was determined with different techniques (Figure 1c).[2,14,16] Thus, the conduction band minimum (CBM) is estimated to be at −4.11 eV with respect to vacuum level (CBM = VBM + E_g). Kelvin Probe measurements were carried out to calculate the work function of the BiI$_3$ thin film, with an approximate value

of -4.73 eV (Figure S2, Supporting Information) which means that BiI$_3$ is slightly n-type, as shown as inset of Figure 1c. Eventually, scanning electron microscopy (SEM) (Figure 1d) reveals a surface morphology with small grains ($\approx$100 nm) not closely-packed (presence of small pores or pinholes) which might limit the PV performance, in agreement with previous reports on the same compound deposited both by solution and vacuum methods.[4,6,16,21,22] At lower magnifications (Figure S3, Supporting Information), the morphology appears more inhomogeneous with the presence of bigger-sized grains. X-ray photoelectron spectroscopy reveals the absence of metallic bismuth on the layers (Figure S4, Supporting Information), usually found at binding energies around 157 eV.[23] Thus, the limited PV performances cannot be attributed to Bi(0) acting as a nonradiative recombination center and limiting thus the performance.[24,25]

For the preparation of bismuth-based solar cells, the choice of the HTL plays a key role in the overall device efficiency. The deep VB of BiI$_3$ strongly limits the availability of an appropriate HTL, as the most commonly used (e.g. PEDOT:PSS, PTAA, Spiro-MeOTAD, PIDT-DFBT) usually present significantly lower

ionization energy.[2,6,21,26–28] Thus, in this work we report the first use of N4,N4,N4′,N4′-tetra([1,1′-biphenyl]-4-yl)-[1,1′:4′,1′-terphenyl]-4,4′-diamine (TaTm) as a suitable hole transport material for bismuth solar cells. Its HOMO level is at −5.4 eV,[29,30] closer to the VBM of BiI_3 than the aforementioned HTLs. On top of an intrinsic layer of TaTm, we incorporate a second layer of TaTm doped with a 6 wt% of 2,2′-(perfluoronaphthalene-2,6-diylidene) dimalononitrile (F_6-TCNNQ) to reduce the series resistance and ensure proper ohmic contact between the HTL and the metal electrode.[30–32] The use of an intermediate thin intrinsic TaTm layer in between the doped TaTm:F_6-TCNNQ layer and the light absorber has proven to be beneficial for the overall performance of lead halide solar cells, as it ensures high fill factors and reduces charge recombination at the interface.[31] In this way, the complete device structure is as follows: ITO/SnO₂/BiI_3/TaTm/TaTm:F_6-TCNNQ/Au (see inset in **Figure 2**a). Both TaTm and F_6-TCNNQ were deposited through thermal evaporation in vacuum, while SnO_2 was grown by ALD, achieving thus a fully vapor processed solar cell.

Table 1. J–V characteristics derived from the BiI_3 film thickness optimization.

Thickness [nm]	V_{oc} [mV]	J_{sc} [mA cm⁻²]	FF [%]	PCE [%]
60	196	3.86	33.1	0.25
80	391	3.15	50.9	0.63
120	281	0.26	41.3	0.03

For the optimization of the BiI_3 layer, three different film thicknesses were explored (60, 80, and 120 nm). Solar cells with thicker layers of BiI_3 usually exhibit low J_{sc} and V_{oc} because of its intrinsic low carrier lifetime and low diffusion lengths.[33] As stated previously by other authors, BiI_3 films required post-deposition annealing to improve its crystallinity and performance. Here, a mild annealing treatment at 50 °C for 10 min was used for all the three thicknesses studied. J–V curves under simulated solar illumination of the three devices are plotted in Figure 2a. **Table 1** collects all the PV parameters extracted from the same curves. The device with 60 nm thick BiI_3 film shows the lowest open-circuit voltage (V_{oc}) and FF of the series, which is likely related with the higher dark current (Figure S5, Supporting Information), resulting from the thin and partially porous BiI_3 layer. With increasing thickness (80 nm), the diode rectification is recovered (FF = 50.9%) and the V_{oc} is enhanced (0.391 V) indicating an overall reduction of charge carrier recombination due to leakage. However, the current density is slightly reduced from 3.86 to 3.15 mA cm⁻², indicating that the charge diffusion length might be limiting current collection already at this thickness.[6] The resulting PCE for the device with 80 nm thick BiI_3 is 0.625%. When an absorber layer thickness of 120 nm is used, the photocurrent is further reduced, again pointing towards a very low charge diffusion length. As a consequence, bulk nonradiative recombination becomes more important, reducing also the V_{oc} of the solar cell.

Therefore, 80 nm was chosen as the ideal thickness for the BiI_3 layer and used for further optimization.

Once the ideal film thickness was set to 80 nm, we explored the role of post-deposition thermal annealing and choice of HTL. When BiI_3 was annealed at 100 °C, all PV parameters increased, reaching a J_{sc} of 3.44 mA cm⁻², a V_{oc} of 0.422 V, and a FF of 51.2%, with an overall PCE of 0.72% (Figure 2b and **Table 2**). On the contrary, annealing at higher temperatures (120 °C) caused the degradation of the thin film and a drastic decrease in absorbance (Figure S6, Supporting Information). Concerning the champion device with a dry thermal annealing treatment at 100 °C, it is worth mentioning that, even though the

Figure 2. a) J–V curve of BiI_3 solar cells by changing the thickness of the layer. Inset showing the solar cell stack is given. b) Comparison of J–V curves with different post-synthesis annealing temperatures and HTLs. Note that dark blue line curves in both panels refer to the same device and are plotted twice for better understanding of different aspects.

Table 2. J–V characteristics derived from the BiI_3 solar cells annealing at different temperatures and changing the HTL.

HTM	Annealing [°C]	V_{oc} [mV]	J_{sc} [mA cm⁻²]	FF [%]	PCE [%]
TaTm/TaTm:F_6-TCNNQ	50	391	3.14	50.9	0.63
	100	422	3.34	51.2	0.72
Spiro-MeOTAD	50	357	4.27	35.2	0.54
	100	386	3.22	36.4	0.45

**ADVANCED
SCIENCE NEWS**
www.advancedsciencenews.com

Energy Technology
Generation, Conversion, Storage, Distribution
www.entechnol.de

PCE is slightly below the current record for a planar configuration (1.21%),[17,18] the fill factor achieved represents the highest value reported so far for a BiI_3 solar cell, which may be ascribed to the better hole extraction by the organic bilayer. The external quantum efficiency (EQE) spectrum (Figure S7, Supporting Information) shows a maximum value around 15% at 600 nm and a cutoff around 1.82 eV, in agreement with previously calculated bandgap energy from optical absorption (1.86 eV).

To further evaluate the role of the HTL, we substituted the TaTm/TaTm:F_6-TCNNQ bilayer with the commonly used solution-processed spiro-MeOTAD. A 300 nm-thick doped-spiro-MeOTAD[34–36] layer was spin-coated on top of BiI_3. As can be seen in Figure 2b and Table 2, the $J–V$ curves show a significant reduction of the FF, a moderate loss of V_{oc} and a small gain of J_{sc} when incorporating spiro-MeOTAD and annealing the BiI_3 films at 50 °C. Increasing the annealing temperature affects negatively the photocurrent and the overall PCE, as compared to the devices using TaTm. Furthermore, we found that the spiro-MeOTAD solution partially dissolves the BiI_3 underlayer leading to a lack of reproducibility. This phenomenon was previously observed by others with BiI_3 layers deposited by different methods.[8]

3. Conclusion

In conclusion, we have shown that the incorporation of a fully-evaporated organic bilayer of TaTm/TaTm:F6-TCNNQ as a deep-HOMO HTL into a BiI_3-based solar cell enhances the hole extraction, achieving a PCE above 0.7% and a fill factor above 51%. It is worth noting that this is achieved in a fully dry process, thus avoiding common toxic solvents such as DMF and employing mild processing (low temperature) conditions. Hence, this paves the way towards the implementation of a truly low-toxicity PV alternative, which nevertheless still requires a significant improvement in efficiency which may come through a better control of the thin film morphology.

4. Experimental Section

Materials: Bismuth iodide (BiI_3, ≥99.998%), chlorobenzene (99.8%, anhydrous), 4-tert-Butylpyridine (TBP) and acetonitrile (anhydrous) were purchased from Sigma-Aldrich. N4,N4,N4′,N4′-tetra([1,1′-biphenyl]-4-yl)-[1,1′:4′,1′-terphenyl]-4,4′-diamine (TaTm) and 2,2′-(perfluoronaphthalene-2,6-diylidene) dimalononitrile (F6-TCNNQ) were provided by Novaled GmbH. 2,2′,7,7′-Tetrakis(N,N-di-p-methoxyphenylamino)-9,9′-spirobifluorene (Spiro-MeOTAD) was purchased from Lumtec. Tris(2-(1H-pyrazol-1-yl)-4-tert-butylpyridine)cobalt(III) tribis(trifluoromethane) sulfonimide (FK 209 Co(III) TFSI salt) was purchased from Dyesol. Lithium bis-(trifluoromethanesulfonimide) (LiTFSI) was purchased from Acros Organics. All chemicals were stored in a nitrogen-filled glovebox and used as received without further purification. Photolithographically patterned ITO coated glass substrates were purchased from Naranjo Substrates.

XRD Characterization: X-ray diffraction was measured with a powder diffractometer Empyrean from Panalytical equipped with CuKα anode operated at 45 kV and 40 mA. Single scans were acquired in the $2\theta = 8°$ to 60° range with a step size of $2\theta = 0.01°$ in Bragg–Brentano geometry in air.

Optical Characterization: UV-visible absorption spectra of the films were collected using a transmission configuration coupled to an Avantes Avaspec-2048L optical detector (Avantes BV). SEM images were acquired using a Hitachi S-4800 Scanning-Electron Microscope, operating at an acceleration voltage of 10 kV.

Air Photoelectron Spectroscopy and Kelvin Probe: The ionization energy of the materials and the work function were determined with an Ambient Pressure Photoemission Spectroscopy Systems (APS02) from KP Technology (KP Technology Ltd, Highlands and Islands, United Kingdom).

Device Fabrication: Deposition and characterization of the thin films were performed inside a clean-room ISO 7 10 000. Glass substrates underwent an extensive cleaning procedure using subsequent sonication in water with soap, deionized water and 2-propanol baths. Then, they were dried with an N_2 flow and placed in a UV Ozone cleaner for 15 min. On top of them, a 30 nm layer of SnOx was deposited by ALD using an Arradiance's GEMStar XT Thermal ALD system integrated into a nitrogen-filled glovebox. For that, the ALD chamber was heated to 90 °C, the bottle containing the Sn precursor (tetrakis(dimethylamino)tin, TDAT) was heated to 60 °C while the bottle of oxidizer (water) was not heated, and the precursor and oxidizer manifolds were heated to 115 and 140 °C, respectively. Prior to deposition, the tubes and valves in the manifolds were degassed three times by performing a series of 30 pulses with the bottles manually closed. The edges of the ITO contacts were protected with Dupont's polyimide Kapton tape and then the substrates were inserted in the ALD chamber, which was then evacuated. The ALD cycle consisted of consecutive purges of TDAT for 550 ms and water vapor for 200 ms, each followed by N_2 purges of 30 and 105 s, respectively, to ensure the complete removal of the precursors from the ALD chamber.

After that, substrates were transferred into a vacuum chamber placed under air conditions and BiI_3 was deposited by thermal evaporation, changing the thicknesses depending on the experiment (60, 80, or 120 nm). Right after, samples were annealed for 10 min at 50 °C or 100 °C when needed. Then, a 20 nm-layer of TaTm and a 40 nm-layer of TaTm:F6-TCNNQ were consecutively deposited in a vacuum chamber inside a nitrogen-filled glovebox. To complete the devices, gold electrodes were evaporated until a thickness of 100 nm.

Spiro-MeOTAD Devices: After the deposition and annealing of the BiI_3 layer, spiro-OMeTAD was spin-coated at 4000 rpm, for 30 s from a chlorobenzene solution containing Li-TFSI, TBP and Co(II)TFSI as dopants. Samples were left overnight in the air to age. Then, gold electrodes were evaporated on top.

Device Characterization: The electrical characterization was performed using a solar with an AM1.5G LED lamp as the light source). For calibrating the lamp, the exact light intensity was determined using a calibrated Si reference diode equipped with an infrared cut-off filter (KG-3, Schott). The layout used to test the solar cells has sixteen equal areas with an active area of 0.05 cm^2. $J–V$ curves were recorded between −0.8 and 1.2 V with 0.01 V steps.

Supporting Information

Supporting Information is available from the Wiley Online Library or from the author.

Conflict of Interest

The authors declare no conflict of interest.

Data Availability Statement

The data that support the findings of this study are available from the corresponding author upon reasonable request.

[1] R. E. Brandt, R. C. Kurchin, R. L. Z. Hoye, J. R. Poindexter, M. W. B. Wilson, S. Sulekar, F. Lenahan, P. X. T. Yen, V. Stevanović, J. C. Nino, M. G. Bawendi, T. Buonassisi, *J. Phys. Chem. Lett.* **2015**, *6*, 4297.

[2] A. J. Lehner, H. Wang, D. H. Fabini, C. D. Liman, C. A. Hébert, E. E. Perry, M. Wang, G. C. Bazan, M. L. Chabinyc, R. Seshadri, *Appl. Phys. Lett.* **2015**, *107*, 1.

[3] B. W. Park, B. Philippe, X. Zhang, H. Rensmo, G. Boschloo, E. M. J. Johansson, *Adv. Mater.* **2015**, *27*, 6806.

[4] U. H. Hamdeh, R. D. Nelson, B. J. Ryan, M. G. Panthani, *J. Phys. Chem. C* **2019**, *123*, 13394.

[5] P. Sebastia-Luna, M. C. Gélvez-Rueda, C. Dreessen, M. Sessolo, F. C. Grozema, F. Palazon, H. J. Bolink, *J. Mater. Chem. A* **2020**, *8*, 15670.

[6] B. W. Williamson, F. T. Eickemeyer, H. W. Hillhouse, *ACS Omega* **2018**, *3*, 12713.

[7] Y. Wang, X. Shi, G. Wang, J. Tong, D. Pan, *J. Mater. Chem. C* **2020**, *8*, 14066.

[8] S. Ma, Y. Yang, C. Liu, M. Cai, Y. Ding, Z. Tan, P. Shi, S. Dai, A. Alsaedi, T. Hayat, *ACS Appl. Mater. Interfaces* **2019**, *11*, 32509.

[9] D. B. Khadka, Y. Shirai, M. Yanagida, K. Miyano, *J. Mater. Chem. C* **2019**, *7*, 8335.

[10] J. Kang, S. Chen, X. Zhao, H. Yin, W. Zhang, M. Al-Mamun, P. Liu, Y. Wang, H. Zhao, *Nano Energy* **2020**, *73*, 104799.

[11] N. F. Coutinho, S. Cucatti, R. B. Merlo, J. M. C. Silva Filho, N. F. B. Villegas, F. Alvarez, A. F. Nogueira, F. C. Marques, *Sci. Rep.* **2019**, *9*, 11785.

[12] M. Khazaee, K. Sardashti, J. P. Sun, H. Zhou, C. Clegg, I. G. Hill, J. L. Jones, D. C. Lupascu, D. B. Mitzi, *Chem. Mater.* **2018**, *30*, 3538.

[13] N. F. Coutinho, R. B. Merlo, N. F. V. Borrero, F. C. Marques, *MRS Adv.* **2018**, *3*, 3233.

[14] I. D. Turjanica, J. Horák, V. M. Benca, D. V. Čepur, *Czechoslov. J. Phys.* **1968**, *18*, 106.

[15] U. H. Hamdeh, R. D. Nelson, B. J. Ryan, U. Bhattacharjee, J. W. Petrich, M. G. Panthani, *Chem. Mater.* **2016**, *28*, 6567.

[16] L. Lin, K. M. Boopathi, J. Ding, C. W. Chu, C. C. Chang, *FlatChem* **2017**, *5*, 18.

[17] D. Tiwari, D. Alibhai, D. J. Fermin, *ACS Energy Lett.* **2018**, *3*, 1882.

[18] B. Yoo, D. Ding, J. M. Marin-Beloqui, L. Lanzetta, X. Bu, T. Rath, S. A. Haque, *ACS Appl. Energy Mater.* **2019**, *2*, 7056.

[19] M. Ruck, *Zeitschrift fur Krist. - New Cryst. Struct.* **1995**, *210*, 650.

[20] D. Mu, W. Zhou, Y. Liu, J. Li, M. Yang, J. Zhuang, Y. Du, J. Zhong, *Mater. Today Phys.* **2021**, *20*, 100454.

[21] A. Kulkarni, T. Singh, A. K. Jena, P. Pinpithak, M. Ikegami, T. Miyasaka, *ACS Appl. Mater. Interfaces* **2018**, *10*, 9547.

[22] S. Sanders, D. Stümmler, P. Pfeifer, N. Ackermann, G. Simkus, M. Heuken, P. K. Baumann, A. Vescan, H. Kalisch, *Sci. Rep.* **2019**, *9*, 9774.

[23] C. D. Wagner, A. V. Naumkin, A. Kraut-Vass, J. W. Allison, C. J. Powell, J. R. Jr. Rumble, NIST Standard Reference Database 20, Version 3.4 (web version) **2003**, http:/srdata.nist.gov/xps/.

[24] M. G. M. Pandian, D. B. Khadka, Y. Shirai, S. Umedov, M. Yanagida, S. Subashchandran, A. Grigorieva, K. Miyano, *J. Mater. Chem. C* **2020**, *8*, 12173.

[25] S. M. Jain, D. Phuyal, M. L. Davies, M. Li, B. Philippe, C. De Castro, Z. Qiu, J. Kim, T. Watson, W. C. Tsoi, O. Karis, H. Rensmo, G. Boschloo, T. Edvinsson, J. R. Durrant, *Nano Energy* **2018**, *49*, 614.

[26] Z. Li, Y. Liang, Z. Zhong, J. Qian, G. Liang, K. Zhao, H. Shi, S. Zhong, Y. Yin, W. Tian, *Synth. Met.* **2015**, *210*, 363.

[27] A. M. Nardes, M. Kemerink, M. M. de Kok, E. Vinken, K. Maturova, R. A. J. Janssen, *Org. Electron.* **2008**, *9*, 727.

[28] J. C. Scott, G. G. Malliaras, W. D. Chen, J. C. Breach, J. R. Salem, P. J. Brock, S. B. Sachs, C. E. D. Chidsey, *Appl. Phys. Lett.* **1999**, *74*, 1510.

[29] H. D. Pham, L. Gil-Escrig, K. Feron, S. Manzhos, S. Albrecht, H. J. Bolink, P. Sonar, *J. Mater. Chem. A* **2019**, *7*, 12507.

[30] J. Avila, L. Gil-Escrig, P. P. Boix, M. Sessolo, S. Albrecht, H. J. Bolink, *Sustain. Energy Fuels* **2018**, *2*, 2429.

[31] C. Momblona, L. Gil-Escrig, E. Bandiello, E. M. Hutter, M. Sessolo, K. Lederer, J. Blochwitz-Nimoth, H. J. Bolink, *Energy Environ. Sci.* **2016**, *9*, 3456.

[32] J. Ávila, C. Momblona, P. Boix, M. Sessolo, M. Anaya, G. Lozano, K. Vandewal, H. Míguez, H. J. Bolink, *Energy Environ. Sci.* **2018**, *11*, 3292.

[33] C. Wu, Q. Zhang, G. Liu, Z. Zhang, D. Wang, B. Qu, Z. Chen, L. Xiao, *Adv. Energy Mater.* **2020**, *10*, 1.

[34] K. T. Cho, S. Paek, G. Grancini, C. Roldán-Carmona, P. Gao, Y. Lee, M. K. Nazeeruddin, *Energy Environ. Sci.* **2017**, *10*, 621.

[35] C. Rodríguez-Seco, M. Méndez, C. Roldán-Carmona, R. Pudi, M. K. Nazeeruddin, E. J. Palomares, *Angew. Chem., Int. Ed.* **2020**, *59*, 5303.

[36] A. D. Jodlowski, C. Roldán-Carmona, G. Grancini, M. Salado, M. Ralaiarisoa, S. Ahmad, N. Koch, L. Camacho, G. De Miguel, M. K. Nazeeruddin, *Nat. Energy* **2017**, *2*, 972.